JACS
JOURNAL OF THE AMERICAN CHEMICAL SOCIETY

Article

pubs.acs.org/JACS

Effect of Isovalent Substitution on the Thermoelectric Properties of the $Cu_2ZnGeSe_{4-x}S_x$ Series of Solid Solutions

Christophe P. Heinrich,[†,‡,∥] Tristan W. Day,[§,∥] Wolfgang G. Zeier,[†,§] G. Jeffrey Snyder,*[,§] and Wolfgang Tremel*[,†]

[†]Institut für Anorganische Chemie und Analytische Chemie der Johannes Gutenberg-Universität, Duesbergweg 10-14, D-55099 Mainz, Germany

[‡]Graduate School Materials Science in Mainz, Johannes Gutenberg-Universität, Staudinger Weg 9, 55128 Mainz, Germany

[§]Material Science, California Institute of Technology, Pasadena, California 91125, United States

Supporting Information

ABSTRACT: Knowledge of structure−property relationships is a key feature of materials design. The control of thermal transport has proven to be crucial for the optimization of thermoelectric materials. We report the synthesis, chemical characterization, thermoelectric transport properties, and thermal transport calculations of the complete solid solution series $Cu_2ZnGeSe_{4-x}S_x$ (x = 0−4). Throughout the substitution series a continuous Vegard-like behavior of the lattice parameters, bond distances, optical band gap energies, and sound velocities are found, which enables the tuning of these properties adjusting the initial composition. Refinements of the special chalcogen positions revealed a change in bonding angles, resulting in crystallographic strain possibly affecting transport properties. Thermal transport measurements showed a reduction in the room-temperature thermal conductivity of 42% triggered by the introduced disorder. Thermal transport calculations of mass and strain contrast revealed that 34% of the reduction in thermal conductivity is due to the mass contrast only and 8% is due to crystallographic strain.

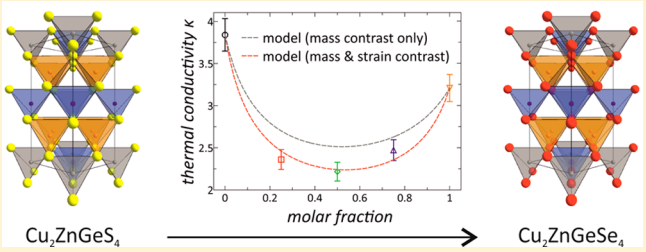

INTRODUCTION

Thermoelectric materials, which convert a temperature difference into a voltage,[1] have proven to be reliable generators of electricity in unmanned space probes[2] and show promise as harvesters of waste heat and as solid-state refrigerators on earth.[3] However, the efficiency of thermoelectric materials must be increased to make them competitive with traditional vapor-compression systems. The efficiency of a thermoelectric material is determined by its dimensionless figure of merit $zT = S^2T/\rho\kappa$, where S is the Seebeck coefficient, T is the absolute temperature, ρ is the resistivity, and κ is the thermal conductivity, which is the sum of a lattice $\kappa_{lattice}$ and an electronic contribution κ_{el}.[4] Following the "phonon-glass, electron crystal" concept introduced by Slack,[5] ways of increasing zT include increasing the so-called power factor S^2/ρ and decreasing the phonon thermal conductivity.

Methods for increasing the power factor include optimization of the carrier concentration,[6] the convergence of electronic bands,[7] and the introduction of "resonant"' states near the Fermi level.[8] Some techniques for reducing $\kappa_{lattice}$ are nanostructuring[9] and alloy scattering in solid solutions.[10] The challenge in increasing the efficiency of thermoelectric materials is the inability to optimize the thermoelectric transport properties independently. Adamantine-like structures,[11] a large class of wide band gap semiconductors, have been intensively studied for photovoltaic[12−14] and magnetic[15] applications and have recently been in the focus of thermoelectric research. Because of their high tolerance toward structural variation, several adamantine materials have been synthesized and the effects of cation substitution on the structure[16] and thermoelectric properties have been investigated.[17−27] Solution-based syntheses of quaternary chalcogenide nanoparticles[28−31] enabled the thermoelectric investigation of nanoscaled chalcogenides.[32−34] However, the possibility of anion substitution to optimize thermoelectric properties has been overlooked so far. It is clear that while atomic substitution can reduce the thermal conductivity (enhanced phonon scattering), it is important to understand its effects on other thermoelectric properties. To this end, we investigated the chemical and thermoelectric changes brought about by replacing Se with S in the model system $Cu_2ZnGeSe_{4-x}S_x$.

EXPERIMENTAL SECTION

Synthesis. Bulk samples of polycrystalline $Cu_2ZnGeSe_{4-x}S_x$ with compositions of x = 0−4 were prepared by solid-state reactions using elemental powders of Cu (Alfa Aesar, 99.999%), Zn (Sigma-Aldrich, 99.995%), Ge (Chempur, 99.99%), Se (Alfa Aesar, 99.999%), and S pieces (Alfa Aesar, 99.999%). The phase purity of all starting materials

Received: October 25, 2013
Published: November 26, 2013

   dx.doi.org/10.1021/ja410753k | J. Am. Chem. Soc. 2014, 136, 442−448

was verified by X-ray diffraction, and all synthetic procedures were carried out under controlled atmosphere in a N_2 drybox. S was carefully resublimed twice under dynamic vacuum to ensure dry and phase-pure conditions. Annealing was performed in evacuated quartz ampules, which were preheated at 1073 K under dynamic vacuum for 5 h to ensure dry conditions. The absence of water was found to be crucial to obtain phase pure reaction products, since the presence of water resulted in the formation of the respective hydrogen chalcogenide, which is able to act as an unwanted transport agent.

The starting elements were thoroughly ground, sealed in quartz ampules, and annealed in a first step at 923 K for 48 h ($x = 0$) and 96 h for $x \geq 1$, respectively. In a following second step, the harvested powders were ground again, resealed, and reannealed for 96 h at 1073 and 973 K, respectively. Heating and cooling rates for all procedures in the horizontal tube furnaces were 5 K/min. The different synthetic temperatures are due to a structural phase transformation at 1063 K, which occurs in the sulfur-containing members of this series.[35] It was found that the second annealing step was necessary to prevent the formation of the binary and ternary compositions. The quartz ampules were 10−12 cm in length and 11 mm inner diameter with a maximum amount of 1.5 g of starting materials within the ampule. This ampule geometry was found to prevent a significant loss of selenium at higher temperatures, indicated by red selenium precipitation present in longer ampules. The obtained powders were hand ground, and the phase purity was verified via standard X-ray diffraction prior to consolidation. Because of the good crystallinity of the binary and ternary side products, impurity levels as low as 0.25% could be detected via quantitative Rietveld refinements. Impure samples were discarded. To ensure sample homogeneity and reproducibility of all measurements, multiple samples of each compound were synthesized and merged to large batches after the phase purity was confirmed by powder X-ray diffraction and Rietveld refinement. Clean batches of powders were used for consolidation into 1−1.5 mm thickness, 12 mm diameter disks at 873 K for 5 h ($x = 0$), 1073 K for 6 h ($x = 1$), and 973 K for 6 h ($x \geq 2$) under a pressure of 40 MPa by induction hot pressing in high-density graphite dies.[36] The resulting samples have more than 95% theoretical density, determined from the mass and geometry of the consolidated disks.

Measurements. X-ray diffraction experiments were performed on a Siemens D5000 powder diffractometer equipped with a Braun M50 position-sensitive detector, Ge (220) monochromator, and Cu Kα_1 radiation, with a step size of 0.0078°. Rietveld refinements were performed with TOPAS Academic V4.125[37] applying the fundamental parameter approach using the crystallographic data from Schäfer and Nitsche as a structure model.[38] Optical reflectance spectra of the fine powdered samples were measured at room temperature on a Varian Cary 5000 UV/vis/near-IR spectrometer equipped with an integrating Ulbricht Sphere and $BaSO_4$ as standard. Optical band gap energies were calculated applying the Kubelka−Munk approximation.[39] Thermal diffusivity was measured using a Netzsch laser flash diffusivity instrument (LFA 457). Prior to thermal diffusivity measurements, samples were spray-coated with a thin layer of graphite to minimize errors in the emissivity and measured under a flowing Ar atmosphere. The data were analyzed using a Cowan model with pulse correction. Heat capacity (C_p) was estimated using the Dulong−Petit approximation ($C_p = 3k_B$ per atom), and theoretical densities were calculated from the molar mass and the refined lattice parameters for each composition. The Seebeck coefficient was calculated from the slope of the voltage vs temperature gradient measurements from chromel−Nb thermocouples under dynamic vacuum.[40] Electrical resistivity was measured using the van der Pauw technique and pressure-assisted contacts under dynamic vacuum.[41] The high resistivity values of some samples resulted in high contact resistances in the van der Pauw measurement system, leading to partially untrustworthy data at lower temperatures. Therefore, data points with large contact resistances and high van der Pauw ratios were discarded. All measurements were performed on multiple samples for each composition. Heating and cooling data are shown in the graphs below.

RESULTS AND DISCUSSION

The chemical and physical properties of $Cu_2ZnGeSe_4$ were reported previously.[26]

Chemical Characterization. Impurity scattering of phonons on grain boundaries is known to strongly influence the thermal conductivity of a thermoelectric material. Therefore, much effort was spent to obtain pure materials with no side phases. All samples were checked for phase purity prior to any measurement. Respective powder X-ray diffraction data of the solid solution series are shown in Figure 1. All reflections can be indexed to the solid solution series limited by the quaternary chalcogenides Cu_2ZnGeS_4 or $Cu_2ZnGeSe_4$, and no secondary phases were observed.

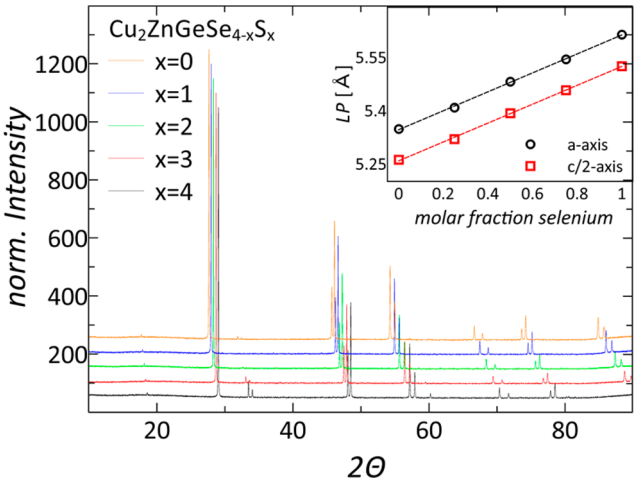

Figure 1. Normalized powder X-ray data of the complete solid solution series $Cu_2ZnGeSe_{4-x}S_x$ with $x = 0-4$ (plots are shifted in intensities for better visibility). The inset shows the refined lattice parameters (LP) a and $c/2$ in Å. Corresponding to Vegard's law, a linear trend of lattice parameters can be seen.

Rietveld refinements of the lattice parameters show an isotropic increase of the a and c axes with increasing selenium content in accordance with Vegard's law (Figure 1, inset).[42] The strict trend in lattice parameters and constant c/a ratio corroborates a homogeneous chalcogen distribution within each sample and the successful substitution of selenium by sulfur in $Cu_2ZnGeSe_{4-x}S_x$, consistent with the work of Wold et al.[35] Refined X-ray data before hot pressing and data obtained from consolidated samples show no significant contribution of texture in these materials. Therefore, we believe that disks of this polycrystalline material are suitable for thermoelectric characterization. Figure 2 shows an example of Rietveld refined powder diffraction data, including profile fit, profile difference, and profile. Refined lattice parameters, c/a ratio, cell volume, and weighted profile R factors of all refinements can be found in Table 1.

Refinements of the nonspecial chalcogen position (Wyckoff position 8i; Figure 3) show a constant increase of the x and y coordinates with increasing selenium content. The z coordinate of the chalcogen position, however, does not change over the solid solution series. In other words, the average chalcogen position is shifting with increasing selenium content toward the center of the unit cell (Figure 3, inset), which results in a partial change in the tetrahedral metal−chalcogen−metal bond angles (Figure 4).

dx.doi.org/10.1021/ja410753k | J. Am. Chem. Soc. 2014, 136, 442−448

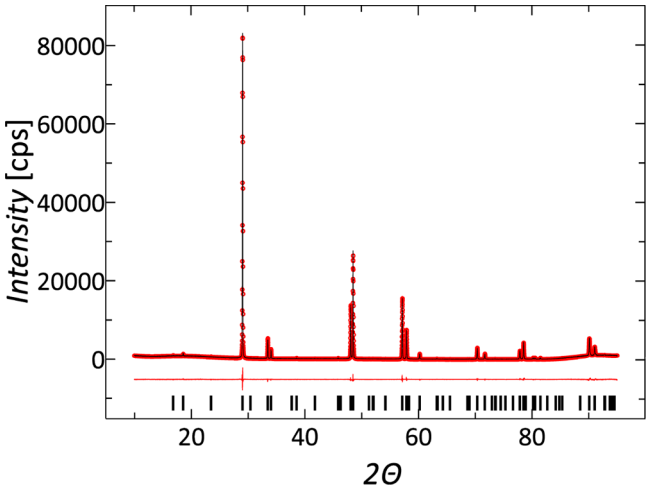

Figure 2. Exemplary powder diffraction data for the Cu_2ZnGeS_4 sample (black solid line), including profile fit (red dotted line), and profile difference (red solid line) from the corresponding Rietveld refinement.

Table 1. Refined Lattice Parameters, c/a Ratio, Cell Volume, and Respective R_{wp} Values

x	a (Å)	c (Å)	c/a	V (Å^3)	R_{wp} (%)
0	5.34808(2)	10.52225(7)	1.967	300.95697(8)	0.064
1	5.40804(2)	10.63897(6)	1.967	311.156856(7)	0.061
2	5.48101(3)	10.78398(7)	1.967	323.966618(8)	0.064
3	5.54397(3)	10.91399(7)	1.968	335.448068(8)	0.066
4	5.61333(2)	11.04886(5)	1.968	348.143763(6)	0.066

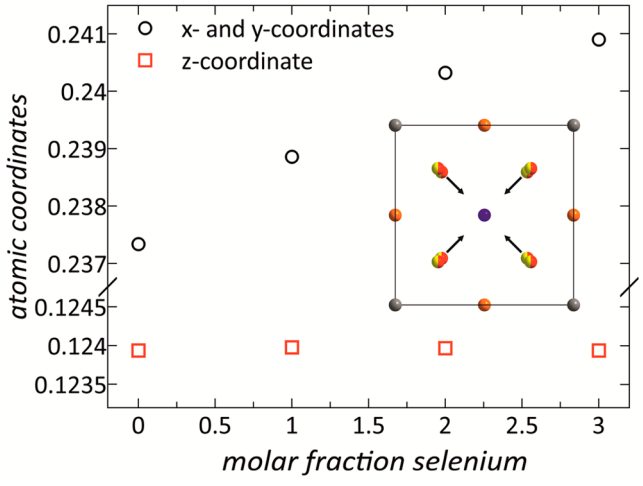

Figure 3. Refined atomic coordinates of the chalcogen position (Wyckoff position 8i). With increasing selenium content the chalcogen position shifts toward the center of the unit cell. The inset shows a projection of the unit cell in the c direction; the arrows indicate the shift of the split chalcogen position (yellow and red) with increasing selenium content.

Metal−chalcogen bond distances increase linearly with increasing selenium content (see the Supporting Information). Bond angles between metals with different z coordinates are either increasing (Cu−X−Zn = 106.93° on average) or decreasing (Ge−X−Cu = 111.12° on average) with increasing selenium content. Angles between metals with the same z coordinate (Cu−X−Cu =109.8° and Ge−X−Zn = 110.47° with X = chalcogen), however, are independent of the selenium

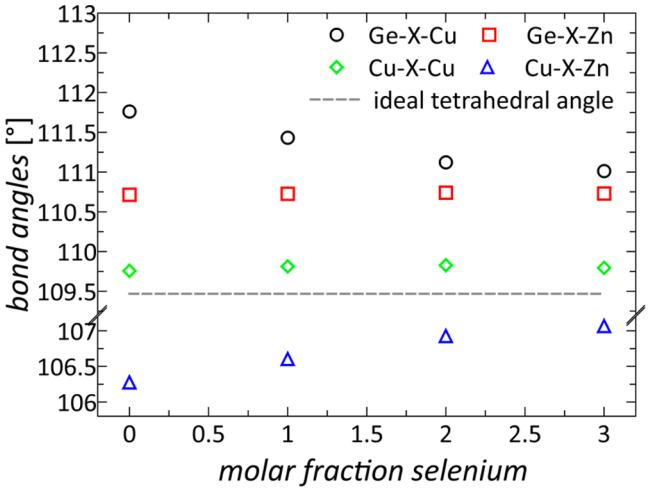

Figure 4. Metal−chalcogenide−metal bond angles in comparison to the ideal tetrahedral angle. Bond angles between metals with different z coordinates (Ge−X−Cu and Cu−X−Zn) change with composition, while angles between metals on the same z coordinate (Ge−X−Zn and Cu−X−Cu) are independent of the composition.

content. Although the maximum change in bond angles is rather small (approximately 1°), it seems reasonable that some amount of crystallographic strain will arise due to the deviation from the ideal tetrahedral angle, which may affect the thermal transport properties (vide infra).

Combined TGA/DSC analysis shows the presence of a subtle exothermic event, as reported previously for $Cu_2ZnGeSe_4$.[26] However, the presence of an exothermic signal throughout the complete solid solution series indicates the occurrence of a phase transition, which has been unobserved so far.[43,44] Interestingly, the phase transition temperature is tunable by the sulfur content and shifts to higher temperatures with increasing sulfur content. Significant weight loss under flowing argon does not occur up to 973 or 1123 K for selenium-rich or sulfur-rich samples, respectively. However, due to significant selenium evaporation under dynamic vacuum at temperatures above 723 K, thermoelectric transport measurements were conducted to a maximum temperature of 673 K to ensure the thermal stability of the samples.

The optical band gap was calculated from the measured diffuse reflectance spectra R using the Kubelka−Munk approximation. Figure 5 shows the absorption spectra plotted as $(\alpha h\nu)^2$ against photon energy. The estimated band gap energies (Figure 5, inset) range from 2.0 to 1.4 eV for Cu_2ZnGeS_4 and $Cu_2ZnGeSe_4$, respectively.

The tunability of band gap energies by anion substitution has been intensely investigated for photovoltaic applications in several of these wide band gap materials[45−49] and can easily be explained by the respective anionic radii. Because of a decrease in anion radius by substitution with sulfur, the orbital overlap is reduced; hence, the dispersion of the bands decreases and the band gap grows energetically with respect to Se-rich samples.

Electronic Transport Properties. The temperature-dependent electrical resistivity of the solid solution series $Cu_2ZnGeSe_{4-x}S_x$ is shown in Figure 6. As expected for undoped, semiconducting, wide band gap materials, the resistivity is rather large and decreases with increasing temperature. We want to stress that all samples are valence precise samples; hence, low charge carrier concentrations are expected, which consequently results in a high resistivity.

dx.doi.org/10.1021/ja410753k | J. Am. Chem. Soc. 2014, 136, 442−448

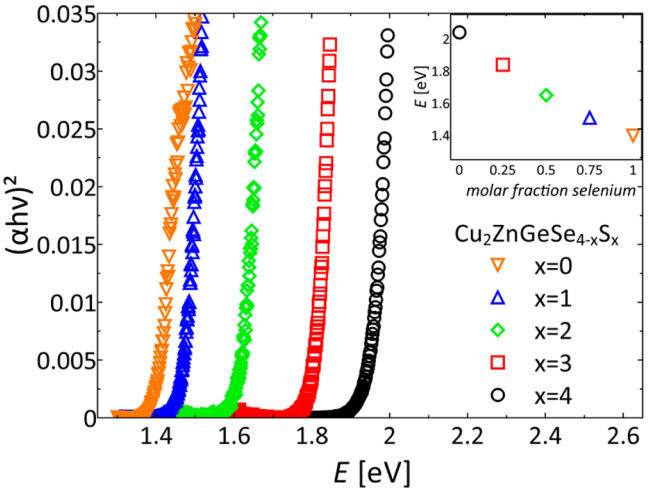

Figure 5. Kubelka–Munk plot from the absorption spectra of the solid solution series $Cu_2ZnGeSe_{4-x}S_x$ with x = 0–4. The inset shows the corresponding extrapolated band gap energies ranging from 2.0 to 1.4 eV.

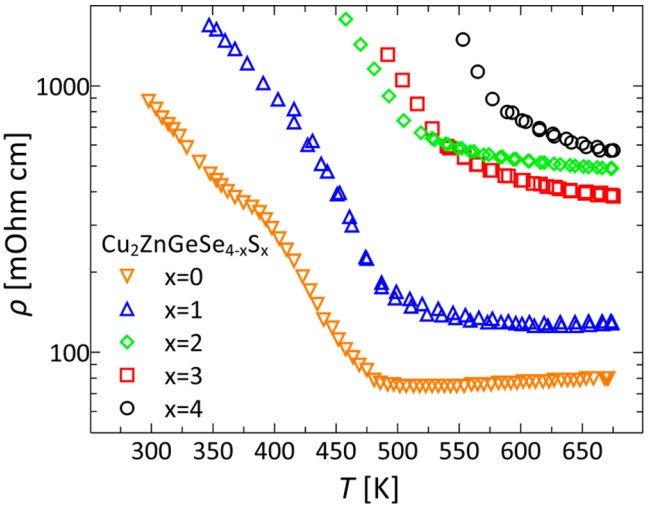

Figure 6. Temperature dependence of the electrical resistivity ρ of the complete solid solution series $Cu_2ZnGeSe_{4-x}S_x$ with x = 0–4, illustrating the trend of higher resistivity with decreasing content of selenium.

Previous work showed that a 10-fold decrease of the resistivity by cation doping is possible.[26] Usually, no great change of the electronic band structure is expected by anion substitution. However, the smaller size of the sulfide anions with respect to the selenide anions leads to a lower degree of covalency and therefore to a higher band effective mass and lower carrier mobility. As a result, the electrical resistivity scales with the sulfur content. The only exception to this trend is the sample with composition $Cu_2ZnGeS_2Se_2$, which shows higher resistivity values above 540 K in comparison to those for Cu_2ZnGeS_3Se. However, previous work showed that control over the carrier concentrations in this kind of material is difficult to achieve due to the inability to control the amount of anion defects.[50] Therefore, extrinsic carriers from intrinsic defects may be the reason for this effect. To obtain lower resistivity values in the undoped quaternary copper chalcogenide $Cu_2ZnGeSe_4$, Selenium could be substituted with tellurium. In addition to the chalcogenide composition, the phase transformation has a significant effect on the electrical resistivity as well. Around the phase transition temperature all samples show a change in the temperature dependence of the resistivity (kink or change in slope). At temperatures below the phase transition temperature the slope of the resistivity–temperature plot is rather steep, as expected from undoped semiconductors. At temperatures higher than the transition temperature a constant or slightly increasing electrical resistivity can be observed, which suggests the existence of a metal to insulator transition, as has been observed for $Cu_2ZnGeSe_4$.[26]

The temperature dependence of the Seebeck coefficient is shown in Figure 7. The Seebeck coefficient ranges from 300 to

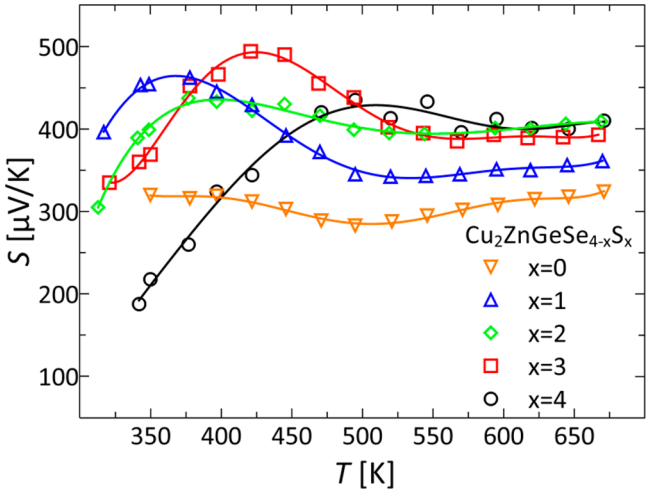

Figure 7. Temperature dependence of the Seebeck coefficient S of the complete solid solution series $Cu_2ZnGeSe_{4-x}S_x$ with x = 0–4. Data points are shown with a line as a guide to the eye.

500 μV/K, and the positive value of the Seebeck coefficient indicates holes as majority charge carriers. Because of the large band gaps and the absence of doped states close to the band edges, no thermal excitation of charge carriers over the band gap and, hence, no contribution of bipolar conduction is to be expected. Therefore, the temperature dependence of the Seebeck coefficient should be constant, which is in good agreement of the measured high-temperature data.

The low-temperature trend of these intrinsic Seebeck compounds suggests that there may be characteristics of extrinsic semiconductor behavior below room temperature, even though the resistivity appears to be of intrinsic semiconductor type. These results indicate that a single parabolic band model is not applicable in these materials, and a more involved model would have to be elaborated to explain the trend in the Seebeck data, which is beyond the scope of this work.

Thermal Transport Properties. The temperature-dependent thermal conductivity of the solid solution series $Cu_2ZnGeSe_{4-x}S_x$ is shown in Figure 8. Every sample exhibits an overall $1/T$ dependence of the thermal conductivity, which indicates Umklapp processes to be responsible for the majority of phonon scattering.[51] However, at the temperature of the aforementioned phase transition a drop in the thermal conductivity can be seen. Usually, the thermal conductivity can be interpreted as the sum of the electronic contribution κ_{el} and the lattice contribution $\kappa_{lattice}$, whereas the electronic contribution is calculated by the Wiedemann–Franz law. Because of the high resistivity, the calculated electronic

dx.doi.org/10.1021/ja410753k | J. Am. Chem. Soc. 2014, 136, 442–448

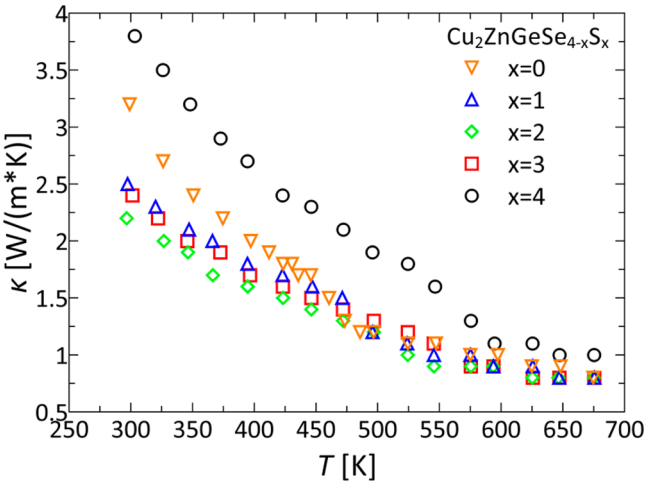

Figure 8. Temperature dependence of the total thermal conductivity κ of the complete solid solution series $Cu_2ZnGeSe_{4-x}S_x$ with $x = 0-4$. Because of the low electrical conductivity the lattice thermal conductivity equals the total thermal conductivity.

contributions to the thermal conductivity are close to 0 over the whole temperature range and the measured total thermal conductivity can be seen as the lattice thermal conductivity.

Therefore, we believe that the chosen system is suitable to study the effect of anion substitution on the reduction of $\kappa_{lattice}$. To avoid the influence of the phase transition, the lattice thermal conductivity was modeled at room temperature, which is considerably below the phase transition temperatures (see Figure 9).

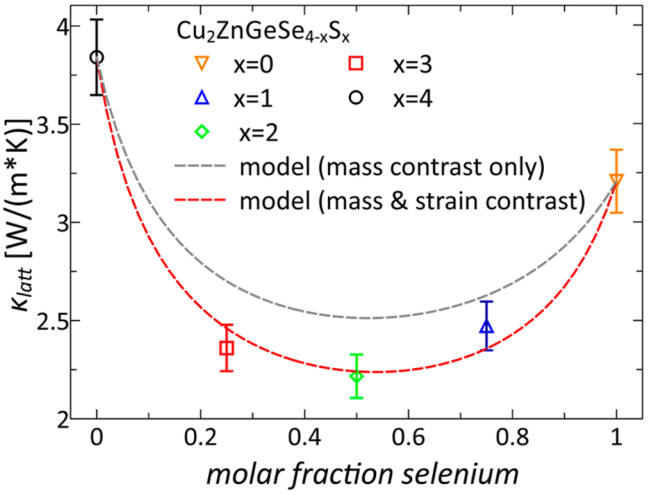

Figure 9. Room-temperature lattice thermal conductivity and modeled lattice thermal conductivities of the complete solid solution series $Cu_2ZnGeSe_{4-x}S_x$ with $x = 0-4$ (gray dashed line, mass contrast only [$\varepsilon = 0$]; red dashed line, mass and strain contrast [$\varepsilon = 36$]) plotted against the molar fraction of selenium.

$Cu_2ZnGeSe_4$ exhibits overall lower thermal conductivity than Cu_2ZnGeS_4, which can be attributed to the larger atomic mass and the softer bonding character of the heavier homologue.[52] However, these are not the only parameters defining the thermal conductivity. In addition to the average anion molar mass, substitution leads to disorder, creating mass contrast and possibly strain contrast in the anion lattice, which both are known to act as point scattering sites for phonons.[10] Taking this into account, it can be seen that the lattice thermal conductivity decreases with increasing disorder on the anion site. The lowest lattice thermal conductivity, therefore, is found in the compound $Cu_2ZnGeS_2Se_2$. At room temperature a total reduction of 42% is obtained for $\kappa_{lattice}$.

Thermal Transport Modeling. To be able to differentiate between the influence of the mass contrast and the strain contrast in the disordered crystal, we calculated $\kappa_{lattice}$ using the Callaway model.[10,52−54] Assuming Umklapp and point defect scattering to be the main scattering mechanisms ($T > \Theta_D$), the ratio of the modeled lattice thermal conductivity of a disordered crystal, $\kappa_{lattice}^{mod}$, and the lattice thermal conductivity of the pure crystal without disorder, $\kappa_{lattice}^{pure}$, is

$$\frac{\kappa_{lattice}^{mod}}{\kappa_{lattice}^{pure}} = \frac{\tan^{-1}(u)}{u} \qquad u^2 = \frac{\pi^2 \Theta_D \Omega}{h v_m^2} \kappa_{lattice}^{pure} \Gamma$$

where u, Ω, h, v_m, and Γ are the disorder scaling parameter, the average volume per atom, the Planck constant, the average sound velocity, and the disorder scattering parameter, respectively. The disorder scattering parameter Γ can be written as

$$\Gamma = \chi(1-\chi)\left[\left(\frac{\Delta M}{M}\right)^2 + \varepsilon\left(\frac{\Delta a}{a}\right)^2\right]$$

where χ, $\Delta M/M$, ε, and $\Delta a/a$ are the molar fraction of selenium, the relative change of atomic mass due to the replacement of selenium by sulfur, the fitting parameter representing the elastic properties of the quaternary chalcogenide, and the local change in lattice parameters resulting from the substitution (pseudocubic approximation $\alpha = V^{1/3}$). The disorder scattering parameter indicates the mass and strain contrast as major contributions for point defect scattering. To calculate $\kappa_{lattice}^{mod}$, the measured thermal conductivities of Cu_2ZnGeS_4 and $Cu_2ZnGeSe_4$ were used as $\kappa_{lattice}^{pure}$, respectively, and the weighted average of both calculations was used for $\kappa_{lattice}^{mod}$. Furthermore, speed of sound measurements were conducted on the complete solid solution series (Figure 10) to obtain the average speed of sound v_m and the Debye temperature Θ_D. A linear trend was assumed, to interpolate the

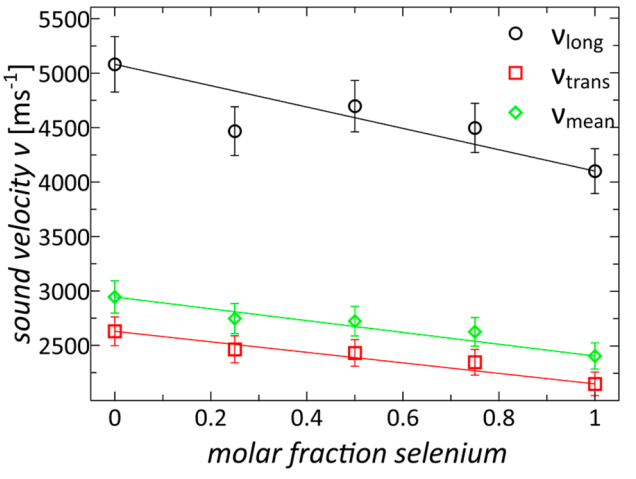

Figure 10. Measured longitudinal, transversal, and calculated mean sound velocity of the complete solid solution series $Cu_2ZnGeSe_{4-x}S_x$ with $x = 0-4$ with the interpolated fit for thermal conductivity calculations.

dx.doi.org/10.1021/ja410753k | J. Am. Chem. Soc. 2014, 136, 442−448

average sound velocities and Debye temperatures of intermediate compositions, which is in good agreement with the speed of sound measurements conducted on samples with intermittent compositions. The calculated Debye temperatures range from 340 to 260 K for Cu_2ZnGeS_4 and $Cu_2ZnGeSe_4$, respectively.

The measured room-temperature thermal conductivity data compared to the modeled thermal conductivities calculated with the contribution of mass fluctuation only (gray dashed line) and with the contribution of mass and strain contrast (red dashed line) can be seen in Figure 9. The best fit ($\varepsilon = 36$) was obtained with the implementation of mass and strain contrast, which is in good agreement with the value of approximately 40 found by Steigmeier and Abeles for germanium−silicon alloys.[55] The calculated thermal conductivities taking only mass contrast into account show a reduction in thermal conductivity of 34%. Considering a total reduction in thermal conductivity of 42%, the further reduction of 8% can be attributed to strain contrast. The good agreement of the fit with the measured data indicates that the reduction of the lattice thermal conductivity within the anion substitution series can easily be calculated using only refined lattice parameters, sound velocities, and thermal conductivity data from the boundary phases, which underlines the power of this modeling approach to predict a possible reduction of $\kappa_{lattice}$ in similar systems.

CONCLUSION

Inspired by the thermoelectric properties of other quaternary chalcogenides, we have synthesized the anion substitution series $Cu_2ZnGeSe_{4-x}S_x$ as a model system for isovalent anion substitutions. Throughout the series a Vegard-like behavior of lattice parameters was shown, which is reflected in a linear trend of bond distances, band gap energy, and speed of sound values. The presence of a phase transformation was confirmed and shown to have a significant effect on the transport properties. Additionally, control over the phase transition temperature by anion substitution could be achieved. Furthermore, a detailed investigation of the room temperature thermal conductivity by isovalent anion substitution revealed a reduction of the lattice thermal conductivity of 42%. Thermal conductivity calculations revealed mass contrast (reduction of 34%) to have a greater influence than strain contrast (reduction of 8%). Finally, due to the successful use of the Callaway model to calculate the lattice thermal conductivity, a powerful tool to predict the lattice contribution to the thermal conductivity in similar substitution series was demonstrated, making it a great way to predict the increase of the figure of merit zT of a thermoelectric compound due to reduced thermal conductivity.

ASSOCIATED CONTENT

Supporting Information

Figure S1, giving refined metal−chalcogen bond distances of the solid solution series $Cu_2ZnGeSe_{4-x}S_x$ with $x = 1-4$, showing a linear trend of increasing bond distances with increasing molar fraction of selenium. This material is available free of charge via the Internet at http://pubs.acs.org.

AUTHOR INFORMATION

Corresponding Author

tremel@uni-mainz.de; jsnyder@caltech.edu

Author Contributions

[‖]These authors contributed equally.

Notes

The authors declare no competing financial interest.

ACKNOWLEDGMENTS

We acknowledge support from the DFG priority program SPP1386 "Nanostructured Thermoelectrics". Further financial support through the Excellence Initative (DFG/GSC 266) is acknowledged by C.P.H. and W.G.Z. W.G.Z. is a recipient of a fellowship of the Carl Zeiss-Stiftung. T.W.D. and G.J.S. acknowledge support from the U. S. Air Force Office of Scientific Research. We gratefully thank Heng Wang (CalTech) for fruitful discussions on thermal conductivity modeling.

REFERENCES

(1) Bell, L. E. *Science* **2008**, *321*, 1457−61.
(2) LaLonde, A. D.; Pei, Y.; Wang, H.; Jeffrey Snyder, G. *Mater. Today* **2011**, *14*, 526−532.
(3) DiSalvo, F. J. *Science* **1999**, *285*, 703−706.
(4) Sootsman, J. R.; Chung, D. Y.; Kanatzidis, M. G. *Angew. Chem., Int. Ed.* **2009**, *48*, 8616−39.
(5) Slack, G. A. *CRC Handbook of Thermoelectrics*; CRC Press: Boca Raton, FL, 1995; p 407.
(6) Snyder, G. J.; Toberer, E. S. *Nat. Mater.* **2008**, *7*, 105−114.
(7) Pei, Y.; Shi, X.; LaLonde, A.; Wang, H.; Chen, L.; Snyder, G. J. *Nature* **2011**, *473*, 66−69.
(8) Heremans, J. P.; Wiendlocha, B.; Chamoire, A. M. *Energy Environ. Sci.* **2012**, *5*, 5510.
(9) Pichanusakorn, P.; Bandaru, P. *Mater. Sci. Eng., R* **2010**, *67*, 19−63.
(10) Wang, H.; LaLonde, A. D.; Pei, Y.; Snyder, G. J. *Adv. Funct. Mater.* **2013**, *23*, 1586−1596.
(11) Schorr, S. *Thin Solid Films* **2007**, *515*, 5985−5991.
(12) Wang, H. *Int. J. Photoenergy* **2011**, *2011*, 1−10.
(13) Wang, K.; Shin, B.; Reuter, K. B.; Todorov, T.; Mitzi, D. B.; Guha, S. *Appl. Phys. Lett.* **2011**, *98*, 051912.
(14) Fan, F.-J.; Wu, L.; Yu, S.-H. *Energy Environ. Sci.* **2013**, *7*, 190.
(15) Guen, L.; Glaunsinger, W. S. *J. Solid State Chem.* **1980**, *35*, 10−21.
(16) Schorr, S.; Hoebler, H.-J.; Tovar, M. *Eur. J. Mineral.* **2007**, *19*, 65−73.
(17) Porras, G.; Quintero, M. *Phys. Status Solidi* **1999**, *215*, 1067−1074.
(18) Shi, X. Y.; Huang, F. Q.; Liu, M. L.; Chen, L. D. *Appl. Phys. Lett.* **2009**, *94*, 122103.
(19) Liu, M. L.; Chen, I.-W.; Huang, F.-Q.; Chen, L.-D. *Adv. Mater.* **2009**, *21*, 3808−3812.
(20) Sevik, C.; Çağın, T. *Appl. Phys. Lett.* **2009**, *95*, 112105.
(21) Liu, M.-L.; Huang, F.-Q.; Chen, L.-D.; Chen, I.-W. *Appl. Phys. Lett.* **2009**, *94*, 202103.
(22) Li, Y.; Meng, Q.; Deng, Y.; Zhou, H.; Gao, Y.; Li, Y.; Yang, J.; Cui, J. *Appl. Phys. Lett.* **2012**, *100*, 231903.
(23) Parker, D.; Singh, D. J. *Phys. Rev. B* **2012**, *85*, 125209.
(24) Kosuga, A.; Plirdpring, T.; Higashine, R.; Matsuzawa, M.; Kurosaki, K.; Yamanaka, S. *Appl. Phys. Lett.* **2012**, *100*, 042108.
(25) Liu, H.; Shi, X.; Xu, F.; Zhang, L.; Zhang, W.; Chen, L.; Li, Q.; Uher, C.; Day, T.; Snyder, G. J. *Nat. Mater.* **2012**, *11*, 422−5.
(26) Zeier, W. G.; LaLonde, A.; Gibbs, Z. M.; Heinrich, C. P.; Panthöfer, M.; Snyder, G. J.; Tremel, W. *J. Am. Chem. Soc.* **2012**, *134*, 7147−7154.
(27) Plirdpring, T.; Kurosaki, K.; Kosuga, A.; Day, T.; Firdosy, S.; Ravi, V.; Snyder, G. J.; Harnwunggmoung, A.; Sugahara, T.; Ohishi, Y. *Adv. Mater.* **2012**, *24*, 3622−3626.
(28) Shavel, A.; Arbiol, J.; Cabot, A. *J. Am. Chem. Soc.* **2010**, *132*, 4514−4515.
(29) Shin, S. W.; Han, J. H.; Park, C. Y.; Moholkar, A. V.; Lee, J. Y.; Kim, J. H. *J. Alloys Compd.* **2012**, *516*, 96−101.

(30) Shavel, A.; Cadavid, D.; Ibáñez, M.; Carrete, A.; Cabot, A. *J. Am. Chem. Soc.* **2012**, *134*, 1438−1441.
(31) Ibáñez, M.; Zamani, R.; Li, W.; Shavel, A.; Arbiol, J.; Morante, J. R.; Cabot, A. *Cryst. Growth Des.* **2012**, *12*, 1085−1090.
(32) Yang, H.; Jauregui, L. A.; Zhang, G.; Chen, Y. P.; Wu, Y. *Nano Lett.* **2012**, *12*, 540−545.
(33) Ibáñez, M.; Cadavid, D.; Zamani, R.; García-Castelló, N.; Izquierdo-Roca, V.; Li, W.; Fairbrother, A.; Prades, J. D.; Shavel, A.; Arbiol, J. *Chem. Mater.* **2012**, *24*, 562−570.
(34) Li, W.; Ibáñez, M.; Zamani, R.; García-Castelló, N.; Gorsse, S.; Cadavid, D.; Prades, J. D.; Arbiol, J.; Cabot, A. *CrystEngComm* **2013**, *15*, 8966.
(35) Doverspike, K.; Dwight, K.; Wold, A. *Chem. Mater.* **1990**, *2*, 194−197.
(36) LaLonde, A. D.; Ikeda, T.; Snyder, G. J. *Rev. Sci. Instrum.* **2011**, *82*, 025104.
(37) Coelho, A. *TOPAS Academic V4.1*; Coelho Software, Brisbane, Australia, 2004.
(38) Schäfer, W.; Nitsche, R. *Z. Kristallogr.* **1977**, *370*, 356−370.
(39) Pankove, J. I. *Optical Processes in Semiconductors*; Dover Publications: New York, 1975.
(40) Iwanaga, S.; Toberer, E. S.; LaLonde, A.; Snyder, G. J. *Rev. Sci. Instrum.* **2011**, *82*, 063905.
(41) Borup, K. a; Toberer, E. S.; Zoltan, L. D.; Nakatsukasa, G.; Errico, M.; Fleurial, J.-P.; Iversen, B. B.; Snyder, G. J. *Rev. Sci. Instrum.* **2012**, *83*, 123902.
(42) Vegard, L. *Z. Phys.* **1921**, *5*, 17−26.
(43) Matsushita, H.; Maeda, T.; Katsui, A.; Takizawa, T. *J. Cryst. Growth* **2000**, *208*, 416−422.
(44) Matsushita, H.; Ichikawa, T.; Katsui, A. *J. Mater. Sci.* **2005**, *40*, 2003−2005.
(45) Haight, R.; Barkhouse, A.; Gunawan, O.; Shin, B.; Copel, M.; Hopstaken, M.; Mitzi, D. B. *Appl. Phys. Lett.* **2011**, *98*, 253502.
(46) Todorov, T. K.; Reuter, K. B.; Mitzi, D. B. *Adv. Mater.* **2010**, *22*, E156−E159.
(47) Tanaka, K.; Fukui, Y.; Moritake, N.; Uchiki, H. *Sol. Energy Mater. Sol. Cells* **2011**, *95*, 838−842.
(48) Wang, K.; Shin, B.; Reuter, K. B.; Todorov, T.; Mitzi, D. B.; Guha, S. *Appl. Phys. Lett.* **2011**, *98*, 051912.
(49) Wei, H.; Ye, Z.; Li, M.; Su, Y.; Yang, Z.; Zhang, Y. *CrystEngComm* **2011**, *13*, 2222.
(50) Zeier, W. G.; Pei, Y.; Pomrehn, G.; Day, T.; Heinz, N.; Heinrich, C. P.; Snyder, G. J.; Tremel, W. *J. Am. Chem. Soc.* **2013**, *135*, 726−32.
(51) Toberer, E. S.; Zevalkink, A.; Snyder, G. J. *J. Mater. Chem.* **2011**, *21*, 15843.
(52) Callaway, J.; von Baeyer, H. *Phys. Rev.* **1960**, *120*, 1149−1154.
(53) Yang, J.; Meisner, G. P.; Chen, L. *Appl. Phys. Lett.* **2004**, *85*, 1140.
(54) Alekseeva, G.; Efimova, B.; Ostrovsk, L. M.; Serebrya, O. S.; Tsypin, M. *Sov. Phys. Semicond.* **1971**, *4*, 1122.
(55) Steigmeier, E.; Abeles, B. *Phys. Rev.* **1964**, *136*, A1149−A1155.